3. DiVincenzo, D. P. Quantum computation. *Science* **270**, 255–261 (1995).
4. Chuang, I. L., Vandersypen, L. M. K., Zhou, X., Leung, D. W. & Lloyd, S. Experimental realization of a quantum algorithm. *Nature* **393**, 143–146 (1998).
5. Kane, B. E. A silicon-based nuclear spin quantum computer. *Nature* **393**, 133–137 (1998).
6. Nakamura, Y., Pashkin, Yu. A. & Tsai, J. S. Coherent control of macroscopic quantum states in a single-Cooper-pair box. *Nature* **398**, 786–788 (1999).
7. Mooij, J. E. *et al.* Josephson persistent-current qubit. *Science* **285**, 1036–1039 (1999).
8. Vandersypen, L. M. K. *et al.* Experimental realization of Shor's quantum factoring algorithm using nuclear magnetic resonance. *Nature* **414**, 883–887 (2001).
9. Leuenberger, M. N. & Loss, D. Quantum computing in molecular magnets. *Nature* **410**, 789–793 (2001).
10. Leuenberger, M. N., Loss, D., Poggio, M. & Awschalom, D. D. Quantum information processing with large nuclear spins in GaAs semiconductors. *Phys. Rev. Lett.* **89**, 207601 (2002).
11. Taylor, J. M., Marcus, C. M. & Lukin, M. D. Long-lived memory for mesoscopic quantum bits. *Phys. Rev. Lett.* **90**, 206803 (2003).
12. Levitt, M. H. *Spin Dynamics* (Wiley, New York, 2002).
13. Wald, K. R., Kouwenhoven, L. P., McEuen, P. L., van der Vaart, N. C. & Foxon, C. T. Local dynamic nuclear polarization using quantum point contacts. *Phys. Rev. Lett.* **73**, 1011–1014 (1994).
14. Gammon, D. *et al.* Nuclear spectroscopy in single quantum dots: nanoscopic Raman scattering and nuclear magnetic resonance. *Science* **277**, 85–88 (1997).
15. Kikkwawa, J. M. & Awschalom, D. D. All-optical magnetic resonance in semiconductors. *Science* **287**, 473–476 (2000).
16. Machida, T., Yamazaki, T., Ikushima, K. & Komiyama, S. Coherent control of nuclear-spin system in a quantum Hall device. *Appl. Phys. Lett.* **82**, 409–411 (2003).
17. Yusa, G., Hashimoto, K., Muraki, K., Saku, T. & Hirayama, Y. Self-sustaining resistance oscillations: Electron-nuclear spin coupling in mesoscopic quantum Hall devices. *Phys. Rev. B* **69**, 161–302 (2004).
18. Salis, G., Awschalom, D. D., Ohno, Y. & Ohno, H. Origin of enhanced dynamic nuclear polarization and all-optical nuclear magnetic resonance in GaAs quantum wells. *Phys. Rev. B* **64**, 195304 (2001).
19. Eickhoff, M., Lenzman, B., Flinn, G. & Suter, D. Coupling mechanisms for optically induced NMR in GaAs quantum wells. *Phys. Rev. B* **65**, 125301 (2002).
20. Nielsen, M. A. & Chuang, I. L. *Quantum Computation and Quantum Information* (Cambridge Univ. Press, Cambridge, 2003).
21. Cohen-Tannoudji, C., Dupont-Roc, J. & Grynberg, G. *Atom-photon Interactions: Basic Processes and Applications* 488–489 (Wiley, New York, 1998).
22. Wokaun, A. & Ernst, R. R. Selective excitation and detection in multilevel spin systems: Application of single transition operators. *J. Chem. Phys.* **67**, 1752–1758 (1977).
23. Leuenberger, M. N. & Loss, D. Grover algorithm for large nuclear spins in semiconductors. *Phys. Rev. B* **68**, 165317 (2003).
24. Ahn, J., Weinacht, T. C. & Bucksbaum, P. H. Information storage and retrieval through quantum phase. *Science* **287**, 463–465 (2000).
25. Grover, L. K. Quantum computers can search arbitrarily large databases by a single query. *Phys. Rev. Lett.* **79**, 4709–4712 (1997).
26. Kronmüller, S. *et al.* New resistance maxima in the fractional quantum Hall effect regime. *Phys. Rev. Lett.* **81**, 2526–2529 (1998).
27. Hashimoto, K., Muraki, K., Saku, T. & Hirayama, Y. Electrically controlled nuclear spin polarization and relaxation by quantum-Hall states. *Phys. Rev. Lett.* **88**, 176601 (2002).
28. Smet, J. H. *et al.* Gate-voltage control of spin interactions between electrons and nuclei in a semiconductor. *Nature* **415**, 281–286 (2002).

....

Seasonal prediction of hurricane activity reaching the coast of the United States

Mark A. Saunders & Adam S. Lea

Benfield Hazard Research Centre, Department of Space and Climate Physics, University College London, Holmbury St Mary, Dorking, Surrey RH5 6NT, UK

....

Much of the property damage from natural hazards in the United States is caused by landfalling hurricanes[1–3]—strong tropical cyclones that reach the coast. For the southeastern Atlantic coast of the US, a statistical method for forecasting the occurrence of landfalling hurricanes for the season ahead has been reported[4], but the physical mechanisms linking the predictor variables to the frequency of hurricanes remain unclear. Here we present a statistical model that uses July wind anomalies between 1950 and 2003 to predict with significant and useful skill the wind energy of US landfalling hurricanes for the following main hurricane season (August to October). We have identified six regions over North America and over the east Pacific and North Atlantic oceans where July wind anomalies, averaged between heights of 925 and 400 mbar, exhibit a stationary and significant link to the energy of landfalling hurricanes during the subsequent hurricane season. The wind anomalies in these regions are indicative of atmospheric circulation patterns that either favour or hinder evolving hurricanes from reaching US shores.

The North Atlantic hurricane season extends from 1 June to 30 November. However, 86% of US hurricane strikes and 96% of US intense (major) hurricane strikes in 1950–2003 occurred after 1 August[5]. The large year-to-year variability in the number of hurricanes making US landfall (range zero to six since 1950) means that skilful seasonal forecasts of activity would benefit a spectrum of decision makers by reducing risk and uncertainty. Seasonal hurricane forecasting was pioneered[6] in the mid-1980s for the North Atlantic. Assessments of seasonal forecast skill for US landfalling hurricane activity have been made for the southeast US from 1 August[4] and for the whole US in September[7]. Work has also examined the probability of US hurricane landfall and damage as a function of the sign and strength of the El Niño/Southern Oscillation (ENSO)[8–11]. However, with one exception[4], none of these studies has claimed skill that is significant, robust and high enough to be practically useful. For example, the hindcast correlation skill for predicting the number of US landfalling hurricanes in September 1950–2000 is only ~0.38 (ref. 7).

Seasonal US landfalling hurricane activity is referenced usually in terms of the numbers of tropical storms, hurricanes or intense hurricanes making US landfall. We introduce the National Oceanic and Atmospheric Administration's Accumulated Cyclone Energy (ACE) index[12] as a single more appropriate measure for categorizing 'seasonal US landfalling hurricane activity'. We call this the US ACE index, and define it as the sum of the squares of hourly maximum sustained wind speeds (in units of knots) from all tropical cyclones over the US mainland (including those that have changed to extratropical) that have winds of at least tropical storm strength. This value is then reduced by a factor of 6 for compatibility with the ACE index at sea, which is computed from wind values every 6 h (ref. 12). The US ACE index is effectively a wind energy index indicating the cumulative wind energy from all US-striking tropical storms, hurricanes and intense hurricanes occurring during a given season. We compute the US ACE index using the maximum sustained wind speed data from the US National Hurricane Center's North Atlantic hurricane database[13].

Our analysis also uses monthly wind data averaged between 925 and 400 mbar (about 750 to 7,000 m above sea level) from the National Center for Environmental Prediction/National Center for Atmospheric Research reanalysis[14] during 1950–2003. The motion of hurricanes is determined by height-averaged winds between these levels[15,16]. US hurricane total (economic) and insured loss data are obtained from ref. 3 (updated economic losses through to the end of 2003 are provided by C. W. Landsea) and from ref. 17 (insured losses for 2000–03 are provided by the US Property Claims Service) respectively for the period 1950–2003. All correlation coefficients (r_{rank}) refer to the Spearman rank correlation coefficient. All statistical significances are two-sided values corrected for serial autocorrelation[18,19].

The US ACE index 1950–2003 is linked significantly to tropospheric height-averaged wind anomalies occurring over North America, the east Pacific and the North Atlantic both before (July) and during the main Atlantic hurricane season. August, September and October are the main months for landfalling hurricane wind energy, with 82% of the annual US ACE index occurring therein. Figure 1 displays for July (Fig. 1a) and

August–October (Fig. 1b) the direction, magnitude and significance of the composite difference in wind anomalies averaged between 925 mbar and 400 mbar for those years when the US ACE index is in its upper and lower quartiles 1950–2003. The vector winds in Fig. 1 are associated with an above-median seasonal US ACE index; wind anomalies of the opposite sign are associated with a below-median seasonal US ACE index.

The composite difference in July height-averaged winds shows several areas of significance. The white boxed regions in Fig. 1a denote six areas (u_1, u_2, u_3, u_4, u_5 and v_1, where u and v refer respectively to zonal (east–west) and meridional (north–south) winds) where the link between the July 925–400 mbar height-averaged wind and the US ACE index 1950–2003 is significant and stationary. Statistical significance is defined as a correlation P-value of <0.1 after correction for serial autocorrelation. Temporal stability is defined as showing statistical significance over each sub-period 1950–76 and 1977–2003. A prominent feature in Fig. 1a is the anticyclonic flow anomaly associated with a strengthened and northward displaced Bermuda high pressure area. When established in July, this feature tends to persist and ridge westwards during

August and September to lie over the US and Canadian eastern seaboards. This leads to on-shore wind anomalies along the US East Coast during August–October (Fig. 1b). As these anomalies will influence the steering of hurricanes, their presence favours an above-median US ACE index year.

Further prominent features in Fig. 1a that favour a subsequent above-median US ACE index are anticyclonic flow associated with increased surface pressure over the Rocky Mountains, and oppositely directed zonal flow anomalies (u_1 and u_2) in the tropical east Pacific. These latter are linked to anomalous zonal gradients in sea surface temperature (SST) caused in part by ENSO. These additional features combine to produce and sustain a cyclonic flow anomaly centred over the Gulf of Mexico during August–October (Fig. 1b). This cyclonic flow strengthens on-shore wind anomalies over Florida and the eastern US Gulf Coast, thereby favouring an above-median US ACE index. July height-averaged wind anomalies opposite to those in Fig. 1a hinder subsequent US hurricane landfall, and herald a below-median US ACE index year.

The identification of tropospheric height-averaged wind anomalies linked significantly and stably to the upcoming US ACE index allows the seasonal predictability of the latter to be assessed. Predictability is computed using cross-validated hindcasts with block elimination[20,21]. This procedure is applied to linear regression models having a single wind index predictor that satisfy the validity assumptions for ordinary least squares linear regression[22,23]. These models are distinguished by the regions contributing to the July height-averaged wind index. Model 1 uses a wind index defined as $u_1 - u_2 + u_3 - u_4 + u_5 - v_1$ with contributions from all six regions. Here each u and v component refers to the area-averaged wind anomaly (Fig. 1a) after normalization by standard deviation. Model 2 uses $u_1 - u_2 - v_1$ as the wind index with contributions from the east Pacific and North America regions only. Model 3 uses $u_3 - u_4 + u_5$ as the index with contributions from the North Atlantic regions only. Skill from these three July 925–400 mbar wind index models is compared to that achievable with perfect *a priori* knowledge of North Atlantic ACE activity
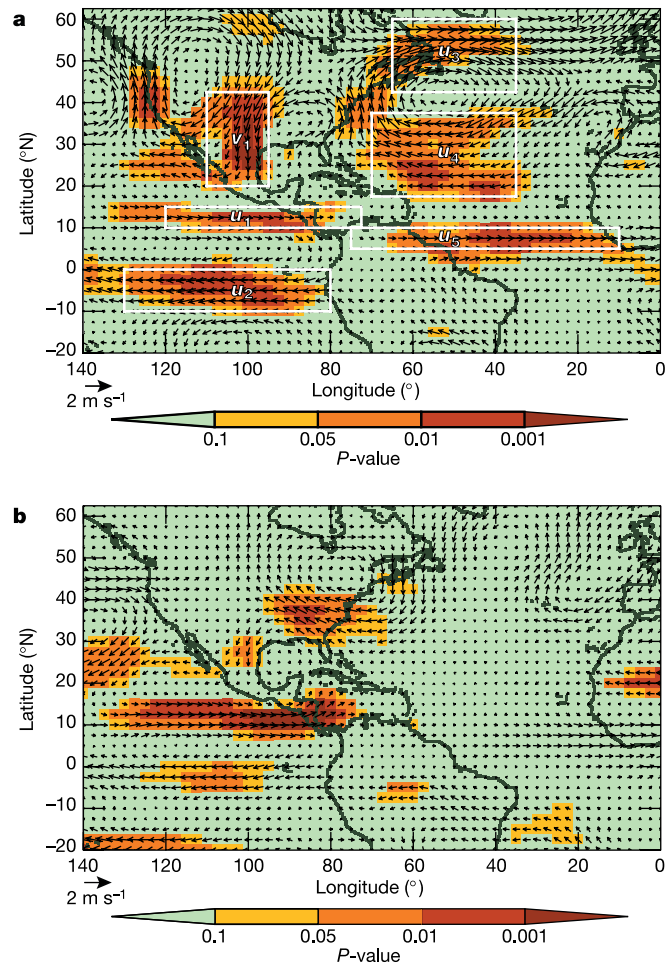

Figure 1 Tropospheric height-averaged wind anomalies linked significantly to above-median seasonal US landfalling hurricane activity 1950–2003. The panels show wind data for July (**a**) and August–October (**b**). Plotted is the difference in vector wind anomalies (averaged between 925 mbar and 400 mbar height) between those subset years when the US ACE index is in its upper and lower quartiles. The significance of the difference in wind magnitude between these subset years is shown by the colour bar. Seasonal predictability of the US ACE index is assessed using a July height-averaged wind index using the six regions marked by white boxes in **a**.

Table 1 Predictive skill for the seasonal US ACE index

Predictor	Period	Hindcast skill and significance		
		MSSS (%)	r_{rank}	P-value
July 925–400 mbar wind index	1950–2003	38	0.67	<0.001
(all regions)	1950–76	40	0.65	0.001
	1977–2003	36	0.70	<0.001
July 925–400 mbar wind index	1950–2003	32	0.68	<0.001
($u_1 - u_2 - v_1$)	1950–76	28	0.68	0.002
	1977–2003	38	0.75	<0.001
July 925–400 mbar wind index	1950–2003	19	0.52	<0.001
($u_3 - u_4 + u_5$)	1950–76	22	0.55	0.004
	1977–2003	14	0.47	0.008
Observed Atlantic total ACE index	1950–2003	18	0.49	<0.001
	1950–76	13	0.38	0.03
	1977–2003	26	0.57	0.003
Observed August–October Niño	1950–2003	0	0.29	0.05
3 SST	1950–76	0	0.26	0.12
	1977–2003	3	0.31	0.12

Table 2 Link between hindcast US ACE index and US hurricane losses

Period	Economic loss		Insured loss	
	r_{rank}	P-value	r_{rank}	P-value
1950–2003	0.48	0.003	0.48	0.003
1950–76	0.43	0.06	0.58	0.03
1977–2003	0.49	0.008	0.37	0.03

(model 4) and of August–October Niño 3 SST (model 5) during the main hurricane season. The US ACE index hindcast skill is assessed using two skill measures: the correlation (r_{rank}) between the hindcast and observed values, and the mean square skill score (MSSS) defined as the percentage reduction in mean square error of the model hindcasts compared to hindcasts made with the 1950–2003 mean or climatology value. MSSS is the skill metric recommended by the World Meteorological Organisation for verification of deterministic seasonal forecasts[21]. P-values are computed from bootstrapped estimates of r_{rank}.

Table 1 shows the hindcast skill from the five models described above for different time periods. Using the July height-averaged wind index (all regions) model, the US ACE index (landfalling hurricane wind energy) is predictable from the 1 August start of the main Atlantic hurricane season with a correlation skill of 0.65–0.70 and a skill improvement over climatology of 36–40%. This skill is significant to $P < 0.001$ over the 1950–2003 period and to

$P = 0.001$ over each 1950–76 and 1977–2003 sub-period. The majority of this skill comes from 925–400 mbar winds over the east Pacific and North America. The strength, significance and stationarity of hindcast skill from the July wind model exceeds (by a factor of two in strength) that achievable from knowing the observed North Atlantic total ACE index at the hurricane season end on 30 November. The low hindcast skill shown by the August–October Niño 3 SST model confirms that ENSO-related wind anomalies are more important than ENSO SST anomalies for US hurricane seasonal predictability. A scatter plot of observed US ACE index versus hindcast US ACE index from the July wind index (all regions) model shows that it anticipates correctly 67% of upper and lower tercile actual values as being upper and lower tercile. Furthermore, the model anticipates correctly 94% of upper tercile actual values as above median and 83% of lower tercile actual values as below median.

The US ACE index hindcasts from the July wind index model offer sound potential for socio-economic benefit. Table 2 shows that the hindcasts are linked significantly ($P < 0.01$) and stably to US hurricane economic loss 1950–2003 (ref. 3) and to US hurricane insured loss 1950–2003 (ref. 17). For both economic and insured losses, $r_{rank} = 0.48$ and $P = 0.003$. These significant links to loss are evident also from Table 3, which compares the hindcast US ACE index values against economic and insured losses stratified by year and above/below median value. For economic loss, the hindcast model correctly anticipates the sign of 74% (40 out of 54) of the above-median and below-median loss years. For insured loss, the hindcast model correctly anticipates the sign of 70% (38 out of 54) of the above-median and below-median loss years. The two-tailed probability of obtaining the 2 × 2 contingency table of US ACE index hindcast and US economic loss by random chance is 0.001 based on Fisher's exact probability test; for hurricane insured loss the probability is 0.006.

A clear beneficiary of the above skill is the insurance industry. Buyers and sellers of reinsurance covers can improve returns over a period of years by up to 30% by using these forecasts[24]. The July 925–400 mbar wind index model performed well in real-time operation in 2004, predicting a US ACE index in the upper quartile for this active and damaging hurricane season (see Atlantic forecast document dated 4th August 2004 at www.tropicalstormrisk.com). Insurers and others would have reduced their losses in 2004 by acting upon the forecast. □

Methods

Serial autocorrelation

We correct for serial autocorrelation to minimize the influence of time series trends and multi-year-to-decadal signal variability on the significance of the deduced hindcast skill[18,19]. We do this by computing the effective number of degrees of freedom in the estimation of the cross-correlation by including autocorrelation coefficients in both input time series out to lags of $N/2$ yr, where N is the time series length.

Significances

The significances in Fig. 1 are computed for each grid cell by selecting two random composite sets of 14 values from the 54-yr 925–400 mbar height-averaged vector wind time series for that grid cell, and computing the wind magnitude difference between these random composites. The selection of values is made with replacement thereby allowing the same value to be picked more than once in a given set. This process is repeated 10,000 times for each grid cell. The random composite wind magnitude differences are displayed in histogram form to give the percentage of the random sets with a wind magnitude difference greater than the actual observed composite difference.

The significances in Tables 1 and 2 are computed by randomly shuffling the 54-yr hindcast/observed US ACE index time series and selecting with replacement a number of hindcast and observed US ACE index pairs corresponding to the number of degrees of freedom after correction for serial correlation in the unshuffled time series. This process is repeated 10,000 times. The correlation from each random set is calculated and the results are displayed in histogram form to give the percentage of the random sets with an r_{rank} greater than the original hindcast r_{rank}.

Predictor selection

The following predictor selection rule is used to select regions and wind components for the July height-averaged wind index. The July area-averaged wind anomaly component

Table 3 Hindcast US ACE index and annual US hurricane damage

	Economic losses				Insured losses		
Year	Hindcast	Loss	US$ million	Year	Hindcast	Loss	US$ million
1992	−	+	44,014	1992	−	+	29,597
1954	+	+	23,302	1954	+	+	18,259
1955	+	+	17,548	1965	+	+	13,922
1965	+	+	16,888	1989	−	+	6,845
1960	+	+	16,236	1964	+	+	5,885
1969	+	+	14,584	1960	+	+	5,707
1972	−	+	14,258	1970	+	+	5,522
1989	−	+	13,705	1979	+	+	5,160
1979	+	+	11,489	1983	−	+	4,729
1961	+	+	9,536	1985	+	+	4,298
1964	+	+	9,377	1961	+	+	4,202
1985	+	+	8,834	1995	+	+	3,710
1999	−	+	6,346	1950	+	+	3,701
2001	+	+	5,579	1969	+	+	3,568
1983	−	+	5,395	1955	+	+	2,946
1995	+	+	4,957	2001	+	+	2,667
1996	+	+	4,635	1996	+	+	2,514
1970	+	+	4,439	1999	−	+	2,430
1998	+	+	4,414	1998	+	+	2,044
1950	+	+	3,732	2003	+	+	1,775
2003	+	+	3,580	1957	−	+	1,422
1957	−	+	3,251	1959	+	+	1,214
1967	+	+	2,726	1972	−	+	1,157
1975	+	+	2,336	1991	−	+	1,117
1991	−	+	2,279	1967	+	+	1,073
1971	+	+	1,612	1975	+	+	946
1994	+	+	1,367	2002	−	+	648
2002	−	−	1,244	1980	−	−	343
1980	−	−	1,151	1956	+	−	332
1974	−	−	953	1966	−	−	255
1959	+	−	594	1984	+	−	162
1956	+	−	466	1976	−	−	155
1968	−	−	425	1971	+	−	147
1976	−	−	408	1974	−	−	143
1958	−	−	296	1968	−	−	117
1951	+	−	242	1953	+	−	113
1966	−	−	219	1986	−	−	84
1963	+	−	197	1952	−	−	67
1984	+	−	173	1993	−	−	57
1973	−	−	126	1997	−	−	50
1997	−	−	123	1988	+	−	23
1988	+	−	116	1977	−	−	14
1981	−	−	102	1963	+	−	5
1978	−	−	100	1987	−	−	1
1990	−	−	99	1951	+	−	0
1993	−	−	85	1994	+	−	0
1952	−	−	84	1981	−	−	0
1962	−	−	56	1990	−	−	0
1977	−	−	44	1973	−	−	0
1986	−	−	39	1978	−	−	0
1953	+	−	37	2000	−	−	0
1982	−	−	36	1962	−	−	0
2000	−	−	30	1982	−	−	0
1987	−	−	18	1958	−	−	0

The comparison is made for the time period 1950–2003. Hindcasts are from the July height-averaged wind index model. Hurricane damage is shown separately in terms of economic and insured losses. The yearly value of each parameter is colour-coded on the basis of whether it is above-median (red, +) or below-median (blue, −). Rows are stratified vertically by loss and referenced by year. Losses are in millions of US dollars at 2003 prices and exposures.

letters to nature

must be linked significantly (correlation P-value <0.1 after correction for serial autocorrelation) to the US ACE index over each sub-period 1950–76 and 1977–2003, and for each year 1950 to 2003 after data excluding a 5-yr block centred on the year in question are excluded. This rule simulates the predictor selection process in an actual forecast situation.

Linear regression modelling

The US ACE index has a positively skewed (generalized Pareto) distribution. To satisfy the assumptions for using ordinary least squares regression, we transform this distribution to a normal distribution using the log(1+US ACE index) transform. We test for normality using the Kolmogorov–Smirnov test. The linear regression modelling is performed on these transformed data to produce hindcasts, which are then transformed back before the hindcast skill is computed. This procedure ensures that the observations are drawn from a normal distribution, and that the hindcast errors are normally distributed with a mean of zero (both requirements of linear regression modelling[22,23]). A one-way analysis of variance (F-test) shows that the variance of the transformed observations and the variance of the hindcast errors are both constant in time (a further assumption of linear regression modelling[22,23]).

The regression modelling is performed with a single predictor variable (the July wind index) rather than as a multiple regression with two or more predictor variables. Multiple regression is found always to give lower hindcast skill, the skill reduction increasing as the number of parameters increases. The single predictor (wind index) approach offers greater skill through better strengthening of the predictive signals and better removal of noise.

Cross-validated hindcasts

Cross-validated hindcasts are made with block elimination[20,21]. The US ACE index of each year is hindcast by training the linear regression model on all data excluding a 5 yr block centred on the year of interest. The block is tapered at the time series ends. Block elimination is used to minimize potential skill inflation that might arise from multi-annual persistence. Cross-validation provides the best available estimate of forecast skill for the 54-yr sample.

Spearman rank correlation

The Spearman rank correlation coefficient is used as a robust and resistant alternative to the Pearson product–moment correlation coefficient[22]. The rank correlation is robust to deviations from linearity in a relationship, and is resistant to the influence of outliers.

1. Benfield Industry Analysis and Research Team, *Catastrophe Losses* (Benfield, London, 2004).
2. Diaz, H. F. & Pulwarty, R. S. *Hurricanes: Climate and Socioeconomic Impacts* (Springer, Berlin, 1997).
3. Pielke, R. A. Jr & Landsea, C. W. Normalised hurricane damage in the United States: 1925–1995. *Weath. Forecast.* **13,** 621–631 (1998).
4. Lehmiller, G. S., Kimberlain, T. B. & Elsner, J. B. Seasonal prediction models for North Atlantic basin hurricane location. *Mon. Weath. Rev.* **125,** 1780–1791 (1997).
5. Gray, W. M., Landsea, C. W., Mielke, P. W. Jr & Berry, K. J. Predicting Atlantic basin seasonal tropical cyclone activity by 1 August. *Weath. Forecast.* **8,** 73–86 (1993).
6. Gray, W. M. Atlantic seasonal hurricane frequency. Part II: Forecasting its variability. *Mon Weath. Rev.* **112,** 1669–1683 (1984).
7. Klotzbach, P. J. & Gray, W. M. Forecasting September Atlantic basin tropical cyclone activity. *Weath. Forecast.* **18,** 1109–1128 (2003).
8. Bove, M. C., Elsner, J. B., Landsea, C. W., Niu, X. & O'Brien, J. J. Effect of El Niño on U.S. landfalling hurricanes revisited. *Bull. Am. Meteorol. Soc.* **79,** 2477–2482 (1998).
9. Pielke, R. A. Jr & Pielke, R. A. Sr. La Niña, El Niño and Atlantic hurricane damages in the United States. *Bull. Am. Meteorol. Soc.* **80,** 2027–2034 (1999).
10. Saunders, M. A., Chandler, R. E., Merchant, C. J. & Roberts, F. P. Atlantic and NW Pacific typhoons: ENSO spatial impacts on occurrence and landfall. *Geophys. Res. Lett.* **27,** 1147–1150 (2000).
11. Lyons, S. W. U. S. tropical cyclone landfall variability 1950–2002. *Weath. Forecast.* **19,** 473–480 (2004).
12. Waple, A. M. *et al.* Climate assessment for 2001. *Bull. Am. Meteorol. Soc.* **83,** S1–S62 (2001).
13. Neumann, C. J., Jarvinen, B. R., McAdie, C. J. & Hammer, G. R. *Tropical Cyclones of the North Atlantic Ocean 1871–1998* (Historical Climatology Series 6–2, National Oceanic and Atmospheric Administration, Asheville, 1999).
14. Kalnay, E. *et al.* The NCEP/NCAR 40-year reanalysis. *Bull. Am. Meteorol. Soc.* **77,** 437–471 (1996).
15. Dong, K. & Neumann, C. J. The relationship between tropical cyclone motion and environmental geostrophic flows. *Mon. Weath. Rev.* **114,** 115–122 (1986).
16. Franklin, J. L., Feuer, S. E., Kaplan, J. & Aberson, S. Tropical cyclone motion and surrounding flow relationships: searching for beta gyres in Omega dropwindsonde datasets. *Mon. Weath. Rev.* **124,** 64–84 (1996).
17. Collins, D. J. & Lowe, S. P. A macro validation dataset for U.S. hurricane models. 217–252 (Casualty Actuarial Society, Winter Forum, 2001); available from CAS at ⟨http://www.casact.org/pubs⟩.
18. Davis, R. E. Predictability of sea surface temperatures and sea level pressure anomalies over the North Pacific Ocean. *J. Phys. Oceanogr.* **6,** 249–266 (1976).
19. Chen, W. Y. Fluctuations in northern hemisphere 700 mb height field associated with the Southern Oscillation. *Mon. Weath. Rev.* **110,** 808–823 (1982).
20. Elsner, J. B. & Schmertmann, C. P. Assessing forecast skill through cross-validation. *Weath. Forecast.* **9,** 619–624 (1994).
21. Standardised verification system (SVS) for long-range forecasts (LRF). *New Attachment II-9 to the Manual on the GDPS (WMO-No. 485)*, Vol. 1 (WMO, Geneva, 2002).
22. Wilks, D. S. *Statistical Methods in the Atmospheric Sciences* (Academic, San Diego, 1995).
23. Freund, R. J. & Wilson, W. J. *Regression Analysis: Statistical Modeling of a Response Variable* (Academic, San Diego, 1998).
24. Hilti, N., Saunders, M. A. & Lloyd-Hughes, B. Forecasting stronger profits. *Glob. Reinsurance* 6–7 (July/August 2004).

....

Active out-of-sequence thrust faulting in the central Nepalese Himalaya

Cameron Wobus[1], Arjun Heimsath[2], Kelin Whipple[1] & Kip Hodges[1]

[1]Department of Earth, Atmospheric and Planetary Sciences, Massachusetts Institute of Technology, Cambridge, Massachusetts 02139, USA
[2]Department of Earth Sciences, Dartmouth College, Hanover, New Hampshire 03755, USA

....

Recent convergence between India and Eurasia is commonly assumed to be accommodated mainly along a single fault—the Main Himalayan Thrust (MHT)—which reaches the surface in the Siwalik Hills of southern Nepal[1–3]. Although this model is consistent with geodetic[4,5], geomorphic[6] and microseismic data[7], an alternative model incorporating slip on more northerly surface faults has been proposed to be consistent with these data as well[8–10]. Here we present *in situ* cosmogenic ^{10}Be data indicating a fourfold increase in millennial timescale erosion rates occurring over a distance of less than 2 km in central Nepal, delineating for the first time an active thrust fault nearly 100 km north of the surface expression of the MHT. These data challenge the view that rock uplift gradients in central Nepal reflect only passive transport over a ramp in the MHT. Instead, when combined with previously reported ^{40}Ar–^{39}Ar data[9], our results indicate persistent exhumation above deep-seated, surface-breaking structures at the foot of the high Himalaya. These results suggest that strong dynamic interactions between climate, erosion and tectonics have maintained a locus of active deformation well to the north of the Himalayan deformation front.

The central Nepalese Himalaya is a textbook example of continent–continent collision, in which the underthrusting of India has been concentrated on several roughly east–west-trending fault zones within a belt about 100 km wide. The northernmost of these fault zones is the Main Central Thrust (MCT), which marks a transition from the high-grade metamorphic Greater Himalayan Sequence in the north to the lower-grade Lesser Himalayan Sequence in the south. Geochronologic data indicate that the MCT is also the oldest structure, with evidence for initial activity on this thrust fault by 23–20 Myr ago[11]. More southerly structures—the Main Boundary Thrust (MBT) and the Main Frontal Thrust (MFT)—developed progressively in a north–south sequence, consistent with observations in foreland fold and thrust belts worldwide[12] (Fig. 1a). Most researchers working in the Nepal orogen assume that recent surface faulting has been concentrated at the trace of the MFT, which defines the southern limit of deformation in the Himalayan system. In this model, the MFT absorbs almost all slip on the MHT. However, this interpretation does not provide a